Research Article | Vol. 32, No. 7 / 25 Mar 2024 / Optics Express 12967
Optics EXPRESS

Nano-imprint lithography of broad-band and wide-angle antireflective structures for high-power lasers

MEHRNAZ MODARESIALAM,[1] NICOLETTA GRANCHI,[2,3] MAREK STEHLIK,[4] CAMILLE PETITE,[4] SORIN DELEGEANU,[1] ANTHONY GOURDIN,[1] MOHAMMED BOUABDELLAOUI,[1] FRANCESCA INTONTI,[2,3] BADRE KERZABI,[1] DAVID GROSSO,[1,5] LAURENT GALLAIS,[4] AND MARCO ABBARCHI[1,6,*]

[1]*Solnil 95 Rue de la Republique, Marseille 13002, France*
[2]*European Laboratory for Non-Linear Spectroscopy (LENS) Via N. Carrara 1, Sesto Fiorentino (FI) I-50019, Italy*
[3]*Department of Physics and Astronomy University of Florence, Italy*
[4]*Aix-Marseille Université, CNRS, Centrale Med, Institut Fresnel, 13013 Marseille, France*
[5]*Aix Marseille Université, CNRS, CINAM, AMUTECH, Marseille, France*
[6]*Université Aix Marseille, CNRS, Université de Toulon, IM2NP, UMR 7334, F-13397 Marseille, France*
[*]*marco.abbarchi@solnil.com*

Abstract: We demonstrate efficient anti reflection coatings based on adiabatic index matching obtained via nano-imprint lithography. They exhibit high total transmission, achromaticity (99.5% < T < 99.8% from 390 to 900 nm and 99% < T < 99.5% from 800 to 1600 nm) and wide angular acceptance (T > 99% up to 50 degrees). Our devices show high laser-induced damage thresholds in the sub-picosecond (>5 J/cm^2 at 1030 nm, 500 fs), nanosecond (>150 J/cm^2 at 1064 nm, 12 ns and >100 J/cm^2 at 532 nm, 12 ns) regimes, and low absorption in the CW regime (<1.3 ppm at 1080 nm), close to those of the fused silica substrate.

© 2024 Optica Publishing Group under the terms of the Optica Open Access Publishing Agreement

1. Introduction

Anti reflection coatings [1,2] (ARCs) are devices that reduce the impact of impedance discontinuity for light propagation across two media featuring a different dielectric constant. They are commercial devices exploited in many applications, including imaging [3] (e.g. on an objective lens [4] or on the glass cover of a C-MOS or CCD detector to enhance the image brightness and reduce the impact of ghost images), photovoltaic [5] (e.g. directly on the absorbing material or atop the glass cover of the solar panel to maximise the light-to-electricity conversion), and extreme UV optics [6,7] (e.g. for high resolution photolithography). Another relevant and challenging field of research on ARCs is high-power lasers: they are relevant to fundamental research (e.g. atomic physics, spectroscopy [8–12]) and they are also used in many applications (e.g. materials processing and inertial fusion [13–22], metrology [23], bio-science and bio-medicine [24], sensing [25,26], communications [27], engines ignition [28], and mining [29]).

It is difficult to quantitatively compare all the solutions that have been developed in many decades of research and development on ARCs devices. Nonetheless, a fundamental distinction between ARCs can be done based on their working principle:

1) they can use destructive interference of light using thin films of appropriate thickness and refractive index [2] (e.g. obtained via chemical vapor deposition [30,31], atomic layer deposition [4], sol-gel chemistry and dip- or spin-coating [32], sputtering [33], electron beam evaporation [34,35]).

#518828 https://doi.org/10.1364/OE.518828
Journal © 2024 Received 12 Jan 2024; revised 8 Mar 2024; accepted 8 Mar 2024; published 22 Mar 2024

Optics EXPRESS

2) they can use 3D resonant structures made of high-refractive index materials that funnel the light in the substrate (e.g. done by lithography and etching [37–39], self-assembly by solid state dewetting [40], nano-imprint lithography of metal oxides [36,41–44]);

3) they can provide a smooth change of refractive index from the surrounding medium to that of the underlying substrate (adiabatic index matching) [16,45–49].

This latter, bio-inspired approach [16,50–53] has become more popular in recent years thanks to its good performances and to the progress in micro- and nano-fabrication. 3D structures can be obtained via top-down lithography [16,48,51,54–65], colloidal self-assembly assisted lithography [56,66,67], nano-imprint lithography of polymers [45,46,49,51] and of metal oxides [42–44,68]. In what follows, we will not consider the case of polymers owing to their lower stability (e.g against rubbing, high temperature, high laser flux) with respect to hard ceramics [68].

When ARCs for high-power laser are considered [69–71], 2D interference coatings and resonant structures are generally less performing: in the first case, the differences in the thermal expansion coefficient of the thin film stack (e.g. with respect to the substrate) result in a rapid degradation of the ARC performances owing to thermal induced strain and consequent fracturing; in the second one, the electromagnetic field intensity is high within the meta-atoms (e.g. owing to the presence of Mie resonances [37,39–41,44,72]) limiting the maximum usable laser power.

For these reasons, the use of ARCs based on adiabatic index matching is nowadays a well-established strategy that extends the usable power range of pulsed and CW lasers. These 3D structures are built with a material having a refractive index close to that of the substrate [43,68] or are directly engraved in the substrate itself [16,37,39,57,59,61–67]. The 3D features of the ARCs have relatively large vertical aspect ratio (height over lateral size $h/d \gtrapprox 1$) a height close or larger than the wavelength of the incident light ($h \gtrapprox \lambda$), high density ($\gtrapprox 10/\lambda^2$) and can be either ordered or disordered.

This kind of ARCs can be tailored to have high transmission and handle high-power lasers: they reduce the impact of the incident light by confining the field intensity in the air gaps between the 3D dielectric elements [73–75]. Recent reports of this approach showcased outstanding performances providing LIDT very close to that of the underlying fused silica (FS) substrate (30 J/cm^2 at 351nm with 8 ns pulses, 74 J/cm^2 at 1053 nm with 4 ns pulses), and reflectance below 1% from 400 to 1100 nm [62–65].

Thus, there are several challenges to address in order to produce efficient ARCs fulfilling the hard requirements for high quality optics, including the sustainability, environmental impact, and costs of the fabrication process used.

In this work we report on the fabrication of broad-band and wide-angle ARCs on glass and FS and their applicability to high-power lasers at visible and near-infrared frequencies. They are obtained via sol-gel spin-coating followed by nano-imprint lithography of metal-oxides (MOx-NIL) [36,43,68]. They are composed of methylated silica (MSA, $Si_4O_7Me_2$) and are shaped as tapered nipple-dimple arrays, a 3D double structure of intercalated pillars and holes arranged in a triangular pattern.

The design of the nipple-dimple structures was not optimized and the masters we used are available *on the shelf* over large surfaces [76]. The substrate was not processed prior to MOx-NIL and the final structures were not cleaned nor laser-conditioned before the LIDT and absorption measurement.

We demonstrate a high total transmission (up to 99.8%) in a broad spectral range, exceeding 500 nm, a wide acceptance angle for both polarizations that feature an almost identical behavior when increasing the beam incidence angle up to 50 degrees with respect to the sample normal. LIDT was tested for sub-ps and ns pulses as well as for CW lasers showing values comparable to those of the underlying FS substrate.

Optics EXPRESS

2. Methods

In this Section we provide a detailed description of the samples preparation and their structural characterization, of the spectroscopic setup for high-power laser measurements (LIDT and absorption), as well as of the finite element methods used for simulations.

2.1. Sol-gel preparation and nano-fabrication of 3D patterns

A detailed description of the MSA sol-gel preparation, mould preparation and the MOx-NIL method used in this work can be found elsewhere [43,68]. The same method was already exploited to fabricate nipple-dimple-based ARCs. In the present work we substantially improved the quality of the nano-imprint quality and tested the devices against high power lasers.

The nickel-based hard masters are provided by Temicon [76] (HT-AR-02 for visible frequency and HT-NIR-02 for near-infrared frequency) and are used to produce a polymeric mould made of PDMS.

The sol-gel solution containing precursors and solvents is spin-coated atop glass and fused FS (Fig. 1(a)). These were previously cleaned using an automatic procedure involving ultrasonic immersion and detergents followed by deionized water, rinsing, and drying. Finally they were treated by oxygen plasma. The substrates are purchased from SINOPTIX (FS, JGS1, double-face polished, 1 inch round wafer, 400 μm thick, surface quality RMS $<$ 5 nm) and SCHOTT (borosilicate glass, double face polished, 1 inch diameter, 500 μm thick).

The equivalent thickness of the 2D layers of MSA used for visible and near-infrared ARCs are respectively of 100 nm and 200 nm after thermal annealing. The amount of initial sol gel spin-coated was set to approximately fill the mould cavities, in order to minimize the residual layer underneath the 3D structures. The corresponding refractive index of the MSA is shown in the Supplement 1 together with those of the glass and FS substrates.

After MOx-NIL by application of the mould, pre-stabilization, demoulding and calcination at high temperature [42,44,68,72,77], the process can be repeated on the back face of the substrate to fabricate a double face ARC (Fig. 1(a)). No particular protection was applied on the front face when printing on the back face.

2.2. Characterization of the optical properties

The spectroscopic characterization from 250 to 2500 nm at normal incidence (0 degrees) of light transmission is performed using a Cary UV-VIS-NIR 5000 spectrophotometer mounting an integrating sphere. The beam size was about 2 cm^2. We estimate an error in the measured intensity of about ±0.1% over the full investigated spectral range (see Supplement 1).

Sol-gel 2D coatings (not imprinted by MOx-NIL) were characterised by ellipsometry (Woollam M2000V) between 400 and 1000 nm by fitting the experimental data with a standard Cauchy model (Supplement 1). The same ellipsometer is used in transmission to measure ss and pp transmission while turning the sample orientation with respect to the beam incidence from 0 to 50 degrees. We estimate an error in the measured intensity of about ±0.25% over the investigated spectral range (see Supplement 1). The beam size was about 0.8 cm^2. This is a relatively small area with respect to the sample extension (about 5 cm^2) and it does not account for its average properties. That is why we compared these results obtained with the ellipsometer with those measured with the spectrophotometer that integrate over a much larger area. The agreement between the two measurements accounts for the reliable information obtained with the ellipsometer.

Optics EXPRESS

2.3. Structural characterization setup

Scanning electron micrographs (collected with a JEOL JSM-7900F SEM) are used for studying the morphology of the sample (Fig. 1(b)-(d) and Supplement 1). The spatial resolution is about 10 nm.

2.4. Laser damage resistance measurements setup

The LIDT is a measure of the maximum laser fluence (J/cm^2 for pulsed laser) or intensity (W/cm^2 for CW lasers) that a device can withstand without damage. By definition, the LIDT is "the highest quantity of laser radiation incident upon the optical component for which the extrapolated probability of damage is zero" [78] (ISO 21254).

The laser damage resistance of the samples (2D flat sol-gel layers and 3D, MOx-NIL based ARCs) has been investigated in three different laser regimes: sub-picosecond, nanosecond and continuous wave (CW). These temporal regimes are representative of the most common high power laser systems used in industrial laser applications.

The setup used for LIDT measurements in ultrashort regime is described in Ref. [79] detailing the test procedures and metrology methods. For the results reported here, the pulses have a nearly Gaussian spatial profile and 500 ±50 fs pulse duration at 1030 nm. The LIDT tests were performed with a beam diameter [80] of 84 μm using a p-polarized laser impinging on the sample with an angle of 51.4 degrees with respect to the normal. The sample under investigation were impacted with laser pulses on different spots using a defined pulse energy. This was increased of 2% to obtain a statistical information. The same measurement process was used for a different number of pulses, sweeping from individual shot up to 1000 shots at a frequency of 10 Hz. The relative incertitude in LIDT measurement is about 4% in the test conditions.

The experimental setup and procedure that were used to measure the LIDT in the nanosecond regime is reported in Ref. [81]. We used an injected Nd:YAG laser (Quantel YG 980) featuring pulses with effective duration of 11 ns [80] at 1064 nm (beam diameter of 106 μm) and at 532 nm (beam diameter of 53 μm). The LIDT is estimated with an R-on-1 ramp test over 20 sites in order to obtain statistical information. The fluctuations of the beam intensity, of its spatial and temporal profiles, lead to a relative incertitude of about 10% in the measured LIDT.

Ex situ investigation of the impacted spots was performed by using a 20× objective lens magnification (Zeiss Axiotech) in a differential interference contrast microscope. The LIDT (for both sub-ps and ns lasers pulses) is estimated considering any observable change of the sample surface as damage. Thus the LIDT was determined as the value of the largest laser energy flux that is below than the lowest flux producing an observable surface modification.

Absorption of the samples was measured using lock-in thermography, with the experimental configuration described in details in Ref. [82]. The system uses a 1 kW CW laser at 1080 nm and a thermal imaging camera to measure the temperature elevation of the sample. Based on coated substrates of the same nature with known value of absorption, it is possible to determine the absorption of the samples in the ppm (part per million) range. The relative incertitude is about 10% in the test conditions. All tests were performed in an air environment at a room temperature of 20 ^{o}C and humidity around 30%.

2.5. Simulations

Finite Difference Time Domain (FDTD) simulations are performed employing the commercial software ANSYS Lumerical. The structure is modelled according to the geometry shown in Fig. 1(e) by imposing periodic boundary conditions. As light source we used a broad band plane-wave $I(f)$ (where f is the frequency) covering the spectral range 350-1200 nm. The beam incidence angle is set at 0 degrees with respect to the sample normal. A 2μm $\times$ 2μm monitor is placed underneath the surface as light detector at a distance of 180 nm with respect to the MSA-substrate interface. The transmission detected by the monitor is calculated as follows:

Optics EXPRESS

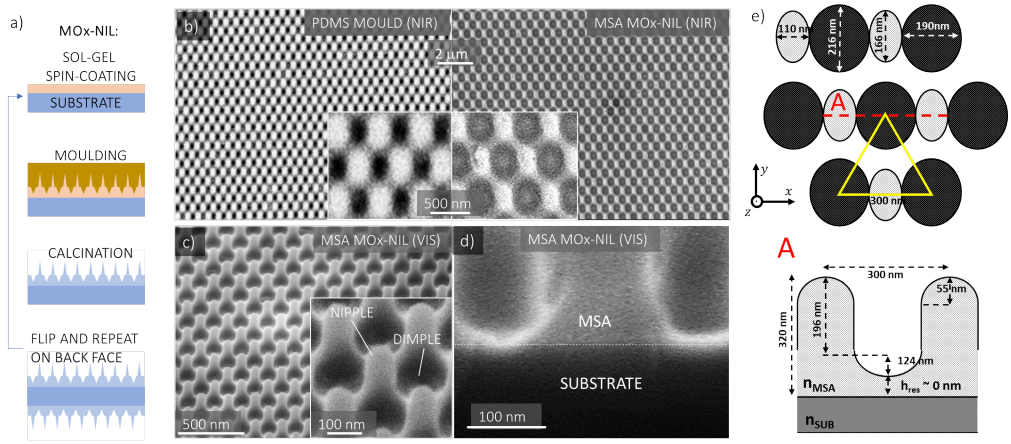

Fig. 1. (a) MOx-NIL fabrication process. (b) Left panel: scanning electron micrograph (SEM) of the PDMS mould obtained from the hard master used for near-infrared frequency devices [76] (NIR). Right panel: MSA-based ARC replica. The insets show a magnified view of the structures. (c) Tilted view at 50 degrees of the MSA replica used at visible frequency (VIS). The inset highlights the nipple-dimple structure. (d) Close-up view showing the cross section of a sample printed on silicon to highlight the thickness of the residual layer. The horizontal, white, dashed line highlights the separation between the MSA-based 3D nano-architectures and the underlying substrate. e) Simplified scheme of the nipple-dimple structure used at visible frequency with the corresponding measures as deduced from SEM. See also in Supplement 1.

$$T(f) = \frac{\frac{1}{2}\int_{monitor} Re(\vec{S}(f)) \cdot \vec{S} dS}{I(f)} \tag{1}$$

where $T(f)$ is the normalized transmission as a function of frequency f, $\vec{S}(f)$ is the Poynting vector and $\vec{S}$ is the surface normal. Field monitors are placed in the xz and yz plane to reconstruct the spatial distribution of the near-field time averaged Poynting vector.

3. Results

3.1. Samples morphology

A detailed description of the ARCs morphology is provided in Fig. 1(b)-(e). We also refer to previous works [68]. Further characterization is provided in the Supplement 1.

Comparing the PDMS mould with the MSA replicas we observe a reduction of about 25% in the nipples diameter and a corresponding increase in the diameter of the dimples (Fig. 1(b)). This is typical of MOx-NIL and is due to the evaporation of the volatile compounds present in the initial sol-gel solution upon stabilization and calcination at high temperature [72,83]. From SEM at tilted angle and in cross section (cleaving a sample printed on a silicon wafer) we measure the main features of the nipple-dimple structures (Fig. 1(c) and (d) and Supplement 1). Their approximated shape is described in detail in Fig. 1(e). These structures sit on a negligibly thin residual layer having a thickness below our instrumental resolution (about 10 nm). This is also confirmed from top view images where the underlying substrate is exposed at the bottom of the dimples (Supplement 1).

We tested the hydrophobicity of our ARCs (Supplement 1): the geometrical analysis of the droplets shows a contact angle exceeding 90 degrees implying that the surface of the samples is hydrophobic [36,48,84]. This is expected for nano-structured surfaces thanks to the presence of

Optics EXPRESS

the pillars and of air inclusions in between the 3D nano-architectures and the air droplets. The hydrofobic nature of the surface is also expected to enhance the self-cleaning properties of the 3D ARC with dust particles that can be absorbed by water droplet that then can roll off the surface.

3.2. Transmission intensity

Light transmission (T) for double face ARCs is determined for both visible and near-infrared frequency cases and accounts for their broad-range character (Fig. 2). ARCs on FS and glass display the same behavior (Fig. 2(a) and (b)). T can reach values as high as 99.8% and has an achromatic character with T > 98% from 400 to 1200 nm and > 96% from 800 to 2500 nm, respectively for the ARC at visible and near-infrared frequencies. Narrowing the spectral range, we observe 99.5% < T < 99.8% from 390 to 900 nm and 99% < T < 99.5% from 800 to 1450 nm, respectively for visible and near-infrared ARCs (Fig. 2(a)-(c)). ARCs on single face display 95.5% < T < 96.2% both at visible and near-infrared frequencies (not shown).

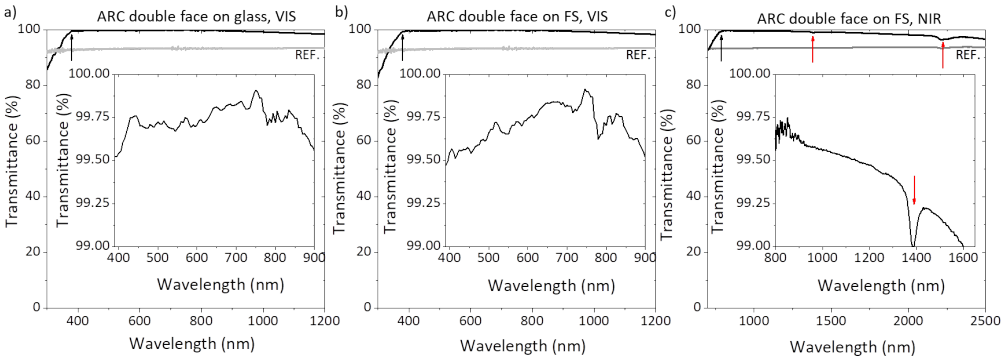

Fig. 2. Transmission measurements with unpolarized light at normal incidence for double face ARC on glass (a) and FS (b) at visible frequency and on FS at near-infrared frequency (c). Each plot reports the FS reference in the main panels and a zoomed plot of the ARC transmission in the insets. Black arrows highlight the wavelength where diffraction start to affect the transmission. Red arrows highlight the presence of light absorption by the FS substrate [85].

Diffraction, springing from the ordered character of these ARCs, is evident below 400 and 800 nm, respectively for the visible and near-infrared frequency devices with a steep reduction in the total transmission. Owing to intrinsic absorption from OH groups in the FS substrate we observe two deeps at about 1380 nm and 2200 nm [85] (Fig. 2(c)).

Transmission measurements at 600 nm resolved in polarization display an almost identical behaviour of ss and pp polarization channels for double face ARCs on FS (Fig. 3): the transmitted intensity stays above 99% up to 50 degrees of beam incidence, accounting for the wide-angle character of our ARCs. These results are representative for all the investigated spectral range: the same measurement performed at different wavelength showcases a similar behaviour and they are not shown. We also display the cases of single face ARC and the bare FS substrate, that show a marked polarization-dependent Fresnel reflection from the flat, unprocessed surfaces. Similar results were obtained for glass at visible frequency and for FS at near-infrared frequency (not shown).

3.3. Laser-induced damage threshold and absorption

LIDT and absorption measurements for different measurement conditions were performed on MSA-based, flat 2D layers (see Supplement 1), on MOx-NIL MSA-based 3D nipple-dimple structures (only one face processed) and on the FS substrate reference (Fig. 4). The LIDTs show

Optics EXPRESS

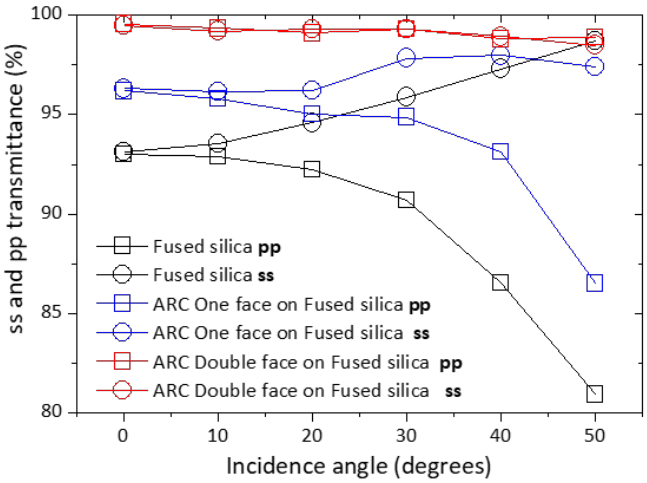

Fig. 3. Transmission measurements for ss and pp polarization at 600 nm for the uncoated FS substrate, single and double face ARC on FS at visible frequency.

very similar values to the substrate accounting for the high quality of our 2D sol-gel coatings and 3D ARCs. Absorption values are close to the ppm, corresponding to about 1 mW of coupled power in the coating for a 1 kW of laser power.

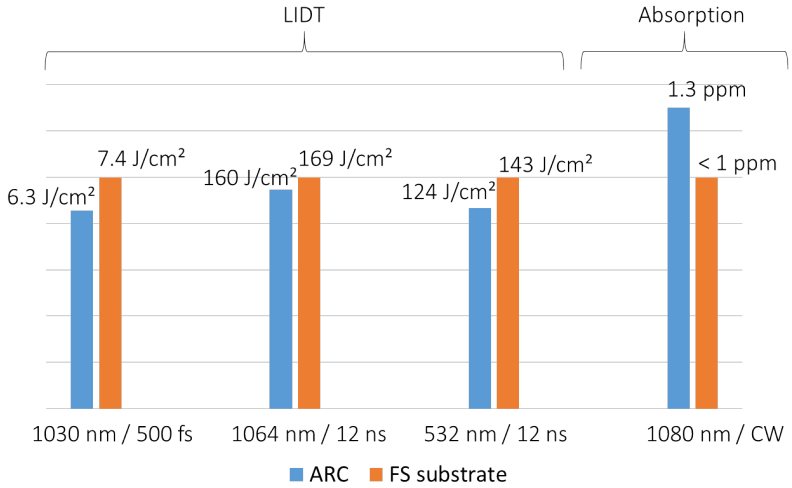

Fig. 4. LIDT and absorption measurements reported for ARCs and Fused Silica substrates (FS). The bar-histograms display the data normalised to the FS substrate values of LIDT and absorption, respectively of the pulsed lasers and for the CW one. The corresponding measured values are reported on the graph and for each case is reported the wavelength of the laser and its pulse length characteristic. Representative examples of R-on-1 LIDT test for the ns laser at 532 and 1064 nm are reported in the Supplement 1.

These results are representative of the intrinsic quality of the ARCs. Nonetheless, for the sake of thoroughness, we mention that a relatively small surface has been tested in these LIDT measurements. Considering the laser spot size the results are not representative of possible extrinsic defects related to the fabrication process that was not performed in a clean-room environment.

Optics EXPRESS

3.4. Finite difference time domain simulations

We simulated the optical response in the far- and near-field by finite element methods of the ARC structure on FS working at visible frequency (Fig. 5) using as a simplified model of the 3D nano-architectures (Fig. 1(e)). For the pattern symmetry considered in this work, the dependence on polarization of the anti-reflective performances at normal incidence is not very relevant, as previously shown [74,86,87]. As such, here we only focus on one polarization oriented along the x direction.

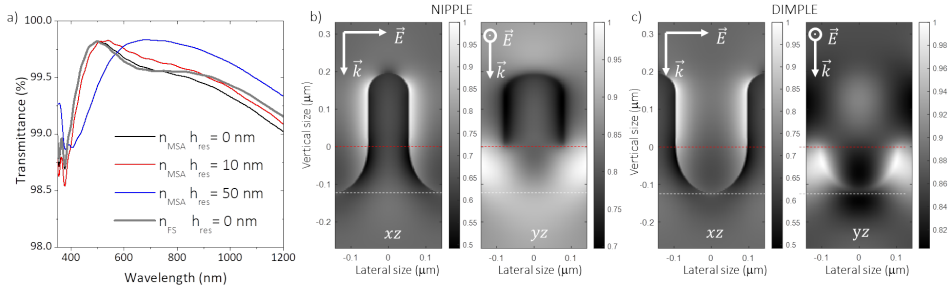

Fig. 5. (a) FDTD simulation of the far-field transmission spectra for nipple-dimple structures composed of MSA (n_{MSA}) with a residual layer of thickness h_{res} = 0, 10 and 50 nm (respectively black, red and blue lines) and for all-FS-based structures (n_{FS}) with h_{res} = 0 nm (gray line). The refractive index of MSA and FS are reported in the Supplement 1. (b) Near-field distribution of the normalized luminance (time averaged Poynting vector $\langle\vec{S}\rangle$, 1 corresponding to white) at 532 nm for the nipple of an MSA-based structure having h_{res} = 0 nm. In the left panel is represented the xz plane, parallel to the electric field polarization $\vec{E}$ and wavevector plane $\vec{k}$; in the right panel is represented the yz plane). The horizontal, white, dashed line highlights the separation between the MSA and the FS substrate. The horizontal, red, dashed line highlights the base of the pillar. (c) Same as (b) for the dimple. The gray scales are different in (b) and (c). In (c) white is 20% smaller than in (b).

The simulated spectra show a high transmission intensity over a broad-band (T > 99% from about 450 nm to above 1200 nm). As for the experimental results, the sharp reduction of T at short wavelength is ascribed to diffraction (Fig. 5(a)).

The effect of the residual layer on T for relatively small values of h_{res} is a progressive shift of the overall spectral response towards longer wavelength, whereas no modulation of the intensity due to interference is observed.

The refractive index of the MSA used for MOx-NIL is lower than that of glass and FS (Supplement 1). Thus, we checked the impact of this parameter simulating a nipple-dimple structure matching the refractive index of the FS substrate (Fig. 5(a)): at short wavelength the effect of a slightly lower refractive index of the MSA with respect to the substrate is negligible, whereas it becomes more important at near-infrared frequency. This could justify the somewhat worse performance of the ARC measured at near-infrared frequency compared to the case at visible frequency (Fig. 2(b) and (c)).

The discrepancies between the experimental results and the simulated transmission spectra are ascribed to slight differences in the geometry of the real structures and those considered in the theoretical model, as well as in the different geometry of the detection in simulations and experiments. However, to a good approximation, the simulated structures catch the main picture emerging from the experiments.

Simulations of the near-field intensity at 532 nm show a larger energy flux (time averaged Poynting vector $\langle\vec{S}\rangle$, or luminance in units of W/m^2) in the air gaps between the structures with respect to the same quantity in the dielectric material, where cold spots are visible (Fig. 5(b) and

Optics EXPRESS

(c), note that, in the yz plane the maximum of $\langle \vec{S} \rangle$ is actually about 20% smaller than that in the xz plane).

4. Discussion

An extensive analysis of the available solutions for ARCs is beyond the aim of this work. Here we consider only the case of adiabatic index matching using 3D structures, that typically provides broader working ranges, wider angular acceptances as well as larger LIDT with respect to interference coatings and resonant particles.

The use of sol-gel coatings for ARCs, including the case of textured ones [55], is well-known [88–90], accounting for their high quality and exploitability for high power lasers. The merit of our work in this respect, is to deliver high quality, printable sol-gel resins that can provide 3D structures with a large vertical aspect ratio with a high homogeneity over each wafer and reproducibility from wafer to wafer. Here we showed a process implemented over 25 mm wafers. Larger ARCs over 100 mm wafers were already reported, accounting for the scalability of the MOx-NIL method [68]. Previous reports on MOx-NIL-based nipple-dimple structures used as ARCs at visible frequencies [68] showed a 20% increase in light reflection after 2000 rubbing cycles with a crock meter (ISO test method 105-F09, pressure 2.08 N/cm^2), as well as a high thermal stability up to 600 ^{o}C, and resilience to aggressive chemical environments. The present results are superior to previous reports [68]. This is mostly due to the minimization of the residual layer, an increased refractive index of the MSA (closer to that of the substrate), a cleaner process (lower defectivity), and a better quality of the MOx-NIL replicas.

Our ARCs provide excellent performances in terms of total transmission and achromaticity in a broad wavelength range and wide-angle acceptance for both polarizations. We compare our results to recent reports of ARCs for high-power lasers (top part of Table 1). Here we only consider the nanosecond regime that is the best established case in the available literature. However, it is important to stress that one original aspect of our study is the complete characterization of the ARCs devices for a broad set of lasers including, beyond the ns case, the sub-ps and CW cases. In Table 1, we also compare our results with ARCs based on adiabatic index matching used for for glass covers (where the LIDT is not addressed), as they are broadly employed well beyond high power lasers applications.

Our results are comparable or superior for transparency, achromaticity and working range with respect to previous reports using adiabatic index matching. Here we performed a full characterization, including glass and FS for ARCs working at visible and near-infrared frequencies, considering also the incidence beam angle and polarization (that is typically not considered for high-power lasers). This allows us to compare with existing results and methods for glass covers with potential use in imaging, displays, detectors, telecommunication, and photovoltaic, showing that our performances are competitive also in these fields.

The observed limitations of our ARCs at short wavelength (at 400 nm and 800 nm, respectively for visible and near-infrared ARCs) spring from diffraction owing to the periodic nature of the 3D MOx-NIL-based structures. This issue can be easily circumvented by using a hard master bearing disordered structures, as already shown in previous reports using dewetted SiGe islands [44,83]. Here, the advantage of the MOx-NIL approach with respect to recent reports [62–64,91] is clear: we can dewet only once ordered [83,92] or disordered structures [44] (including the relevant case of hyperuniform ones [93]) and use this as a hard master to print via MOx-NIL the ARCs, repeating them *ad libitum*.

As for the LIDT, a straightforward and quantitative comparison between different reports is not possible, owing to the critical dependence of this quantity on many parameters (e.g. laser beam spatial shape and size, pulse shape and duration, polarization) [70,96–98]. Nonetheless, a reasonable comparison can be done by monitoring the performance loss of the ARC with respect

Optics EXPRESS

Table 1. Summary of optical performances of ARCs for high-power laser and glass covers. We compare the total transmission T (or reflection R), the performance in angle and the LIDT. Here we only focus on the ns laser case For sub-ps and CW regime we refer to Figure 4. At the top of the table are reported the results of this work. In the middle part those studying the LIDT and in the bottom part the data of ARCs for glass covers (where the LIDT was not addressed).

Ref., Subs.	Method	Range	T,R(λ)	T, R(θ) 0-50 deg.	LIDT J/cm^2 ARC (Subs.), [λ, Pulse length]
This work, Glass	MOx-NIL	390-900 nm	T>99.5 %	T > 99%	/
This work, FS		390-900 nm	T>99.5%	T>99%	124 (143), [532 nm, 11.7 ns]
This work, FS		800-1600 nm	T>99%	T>98%	160 (169), [1064 nm, 11.7 ns]
[57] FS	UV-Lithog.	820-1180 nm	T>99.6%	/	100 (138), [1060 nm, 10 ns]
[94] FS	Holog. Lithog.	400-900 nm	T>99%	/	30 (38), [1064 nm, 12 ns]
[64] FS	Dewet. Lithog.	351 nm	R=0.37%	/	20 (22), [351 nm, 5 ns]
[62] FS	Dewet. Lithog.	325-500 nm	R<1%	/	30 (47), [351 nm, 8 ns]
		900-1100 nm	R<0.5%	/	74 (81), [1053 nm, 4 ns]
[55] FS	Sol-gel and ICP	380-700 nm	R<0.6%	/	26 (32), [351 nm, 5 ns]
[75] FS	Holog. Lithog.	980-1220 nm	T>99%	/	56 (60), [1064 nm, 10 ns]
[65] FS	Dewet. Lithog.	350-1300 nm	R<1.2%	R<0.2%	/
[36] Glass	MOx-NIL	400-1000 nm	R<3%	R<1%	/
[60] FS	Mask-less RIE	300-1000 nm	R<1%	R<3%	/
[58] FS	Mask-less RIE	300-1000 nm	T>98%	R<5%	/
[95] FS	Block-cop.	400-1050 nm	R<0.4%	/	/
[48] FS	Interf. lithog.	600-1700 nm	T>98%	T>97%	/

to those of the bare substrate: the best ARCs showcase an LIDT that is very close to that of the underlying material.

In the case of the sub-ps regime (1030 nm, 500 fs), the measured LIDT are close to the substrate value. When corrected from the angle of incidence ($\cos(51^o) = 0.63$), the LIDT of ARCs coatings is about 4 J/cm^2, very close to values measured on silica films made by PVD (such as IBS [97]). This LIDT value implies that the intrinsic limitations of the material, related to its bandgap, has been reached.

In the ns regime we also tested the 2D flat layers composed of MSA deposited on FS: at 1064 (532) nm for 11.7 ns pulses they show an LIDT of 172 ± 17 (125 ± 12) J/cm^2 (Supplement 1). Within the experimental error these values are equivalent to the bare FS substrate that at 1064 (532) nm shows an LIDT as high as 169 ± 17 (143 ± 14) J/cm^2. For MOx-NIL-based ARCs tested in the ns regime we observe a loss of 13% at 532 nm, and of 6% at 1064 nm with respect to the FS substrate, that is not far from what can be obtained with lithographic methods (LIDT loss about 6-10%, Table 1).

In the CW regime the laser damage is caused by heating or mechanical failure owing to thermally-induced stress in the coating and in the substrate via localized increase in absorption. Thus, the absorption value is the main parameter to evaluate the laser damage resistance. Our ARCs exhibit an absorption value close to 1 ppm, similar to that of the FS substrate [99,100], further accounting for the low-loss character of our materials and ARCs and their explotability for high power laser applications.

Our results were obtained without any optimization of the ARC design: filling fraction, vertical aspect ratio and side-walls slanting were not considered [59] as well as the shrinking of the MSA

Optics EXPRESS

upon calcination [72]. We just used *on the shelf* masters, commercially available over 250 mm x 250 mm [76], leaving room for improvement with a dedicated design. Through FDTD simulations we infer that the field redistribution outside the MSA material and atop the FS substrate is the key mechanism for the large increase in the LIDT of our ARCs, as previously suggested [73,74]. This observation led to the optimized shape of 3D structures by fine tailoring the vertical aspect ratio, filling fraction and side-walls slanting [59]. Thus, in spite of the non-optimal geometry of our ARCs, the measured optical parameters, LIDT, absorption, and the near-field simulations, account for the fact that the nipple-dimple geometry is favourable for high quality ARCs and adapted to high power lasers.

For the sake of thoroughness, we mention that the use of relatively small laser spot size and a R-on-1 ramp test, provides a rough estimation of the LIDT owing to the low defectivity of the sample and unintentional conditioning of the sample surface by the laser. In the merit of this, we verified that in the sub-ps regime using 1 to 1000 pulses per site, does not significantly modify the LIDT of the MSA material, suggesting a minor effect of laser conditioning (not shown). However, this kind of R-on-1 ramp test is not complete and a more precise assessment of the real LIDT will require larger impacted areas using raster scan and S-on-1 measures to assess the fatigue (incubation) effect. In the same context it is worth stressing that changes in the experimental setup can lead to very large differences (up to a factor of 100) in the measured LIDT for the FS substrate [101].

Top-down lithographic methods provide excellent ARCs and LIDT performances [102]. Among them, direct engraving the substrate after solid-state dewetting of thin Au [62–64] or Pt [65,91] films has emerged as one of the best options, delivering an LIDT of only 6% short of the FS substrate, although assessed only for ns lasers. The forte of this method is the possibility to process arbitrarily large surfaces with a self-assembled etching mask. Leveraging on the intrinsically stochastic nature of the dewetting process, the islands feature a rather large distribution of size and shape and their organization is disordered. As such, it avoids diffraction, rendering more achromatic the spectral response of the ARC [58,60]. However, the dewetting instability provides islands with size and average inter-particle distance set by the initial thickness of the film and by the surface energy density [40,83,92,93,103]. As such, the filling fraction (area fraction occupied by the islands relative to the underlying area of the substrate) is fixed. To adjust this parameter, several cycles of re-deposition of Au or Pt are necessary prior to etching the substrate [64]. All these fabrication steps must be repeated for every device rendering the overall process very long and expensive. In order to increase the LIDT, the FS substrates are pre-treated and before use, the ARCs obtained via etching need for a laser conditioning or rapid thermal annealing to remove any plasma-inducing precursors [63] and potential defectivity springing from surface and sub-surface contaminants [75,104].

Beyond performances, hard requirements for the widespread use of ARCs (and more generally nano-devices) are their implementation over large surfaces at sustainable costs, with low environmental impact and low carbon footprint, while limiting the use of critical raw materials. In this respect, top down "subtractive" methods (e.g. substrate-engraving by top-down etching [16,37,39,57,58,60–67]) typically use many chemicals, toxic resists, high-power UV-light sources, hard lithographic masks made of precious metals such as Au and Pt that cannot be recycled, resulting in a negative impact on the environment and the working conditions and safety of the employees producing the ARCs. The use of fluorinated gases for FS and glass etching (e.g. SiF_4, CF_3, and C_4F_8 [62,64,65,91,105]) poses many concerns and many countries (e.g. in EU [106]) will soon ban their use owing to their negative impact on the ozone layer.

It is in this context that MOx-NIL stands as a viable and sustainable solution for high-quality ARCs as well as for many other applications: it delivers a finalised device in a few fabrication steps (a sample can be prepared in about 30 minutes [68]) reducing defectivity and production costs, it does not use any precious metal as mask, it avoids the use of toxic resist and fluorinated

Optics EXPRESS

gases, it saves about 90% energy with respect to deep-UV high power lamps [107] thus cutting on CO_2 production, and it is compatible with plate-to-plate and roll-to-plate industrial processing, potentially increasing the production yield.

We tested the reproducibility of the MOx-NIL process by using the same PDMS mould several times to print the ARCs. Monitoring the transmission, we did not measure any performances loss after 7 replicas, suggesting that the same mould can be re-used a few tens of times. This detail, together with all the advantages of MOx-NIL over conventional methods involving etching, corroborates the picture of a sustainable process for ARCs over large surfaces.

5. Conclusion

In conclusion we demonstrated highly performing broad-band and wide-angle ARCs using nano-imprint lithography of metal-oxides providing a comprehensive assessment of their optical properties at visible and near-infrared frequencies including the total transmission, angular acceptance and resilience against high power lasers in the sub-ps, ns and CW regimes. Their performances are comparable or superior to the existing state of the art, showcasing the exploitability of our devices for high-power lasers. The high tolerance to wide incidence angles of our devices accounts also for their applicability as glass covers, extending their use to imaging, lightening, detection, telecommunication, photovoltaic and quantum optics. The sustainability and simplicity of our fabrication process together with its compatibility with plate-to-plate and roll-to-plate fabrication account for its high market readiness.

Disclosures. The authors declare no conflicts of interest.

Data availability. Data underlying the results presented in this paper are not publicly available at this time but may be obtained from the authors upon reasonable request.

Supplemental document. See Supplement 1 for supporting content.

References

1. J. Fraunhofer and J. v. F. G. Schriften, "Munich," (1888).
2. J. A. Dobrowolski, D. Poitras, and P. Ma, "Toward perfect antireflection coatings: numerical investigation," Appl. Opt. **41**(16), 3075–3083 (2002).
3. H. K. Raut, V. A. Ganesh, A. S. Nair, *et al.*, "Anti-reflective coatings: A critical, in-depth review," Energy Environ. Sci. **4**(10), 3779–3804 (2011).
4. K. Pfeiffer, L. Ghazaryan, U. Schulz, *et al.*, "Wide-angle broadband antireflection coatings prepared by atomic layer deposition," ACS Appl. Mater. Interfaces **11**(24), 21887–21894 (2019).
5. A. S. Sarkın, N. Ekren, and Ş. Sağlam, "A review of anti-reflection and self-cleaning coatings on photovoltaic panels," Sol. Energy **199**, 63–73 (2020).
6. Q. Huang, V. Medvedev, and R. van de Kruijs, "Spectral tailoring of nanoscale euv and soft x-ray multilayer optics," Appl. Phys. Rev. **4**(1), 1 (2017).
7. Y. Chen, D. Xu, and K. Xu, "Optoelectronic properties analysis of silicon light-emitting diode monolithically integrated in standard cmos ic," Chin. Phys. B **28**(10), 107801 (2019).
8. W. D. Phillips, J. V. Prodan, and H. J. Metcalf, "Laser cooling and electromagnetic trapping of neutral atoms," J. Opt. Soc. Am. B **2**(11), 1751–1767 (1985).
9. S. D. Jackson, "Towards high-power mid-infrared emission from a fibre laser," Nat. Photonics **6**(7), 423–431 (2012).
10. A. Pospori, C. A. Marques, and O. Bang, "Polymer optical fiber bragg grating inscription with a single uv laser pulse," Opt. Express **25**(8), 9028–9038 (2017).
11. L. C. Silva, C. A. Marques, M. E. Segatto, *et al.*, "Stable self-pulsing regime in a brillouin ring fiber laser cavity," Laser Phys. **31**(5), 055103 (2021).
12. W. Sibbett, A. Lagatsky, and C. Brown, "The development and application of femtosecond laser systems," Opt. Express **20**(7), 6989–7001 (2012).
13. C. J. Stolz, M. Caputo, A. J. Griffin, *et al.*, "Bds thin film uv antireflection laser damage competition," in *Laser-Induced Damage in Optical Materials: 2010*, vol. 7842 (SPIE, 2010), pp. 62–67.
14. C. J. Stolz and R. A. Negres, "Ten-year summary of the boulder damage symposium annual thin film laser damage competition," Opt. Eng. **57**(12), 1–121910 (2018).
15. H. Injeyan and G. D. Goodno, *High power laser handbook* (McGraw-Hill Education, 2011).
16. L. E. Busse, J. A. Frantz, and L. B. Shaw, "Review of antireflective surface structures on laser optics and windows," Appl. Opt. **54**(31), F303–F310 (2015).

Optics EXPRESS

17. D. Flamm, D. G. Grossmann, and M. Sailer, "Structured light for ultrafast laser micro-and nanoprocessing," Opt. Eng. **60**(2), 025105 (2021).
18. R. Crafer and P. J. Oakley, *Laser processing in manufacturing* (Springer Science & Business Media, 1992).
19. S. Katayama, *Handbook of laser welding technologies* (Elsevier, 2013).
20. J. Nilsson and D. N. Payne, "High-power fiber lasers," Science **332**(6032), 921–922 (2011).
21. J. H. Martin, B. D. Yahata, and J. M. Hundley, "3d printing of high-strength aluminium alloys," Nature **549**(7672), 365–369 (2017).
22. H. A. Atikian, N. Sinclair, and P. Latawiec, "Diamond mirrors for high-power continuous-wave lasers," Nat. Commun. **13**(1), 2610 (2022).
23. G. Marra, R. Slavík, and H. S. Margolis, "High-resolution microwave frequency transfer over an 86-km-long optical fiber network using a mode-locked laser," Opt. Lett. **36**(4), 511–513 (2011).
24. J. R. Unruh, E. S. Price, and R. G. Molla, "Two-photon microscopy with wavelength switchable fiber laser excitation," Opt. Express **14**(21), 9825–9831 (2006).
25. N. Leindecker, A. Marandi, and R. L. Byer, "Octave-spanning ultrafast opo with 2.6-6.1 μm instantaneous bandwidth pumped by femtosecond tm-fiber laser," Opt. Express **20**(7), 7046–7053 (2012).
26. D. K. Killinger and A. Mooradian, *Optical and laser remote sensing*, vol. 39 (Springer, 2013).
27. D. Cornwell, "Space-based laser communications break threshold," Opt. Photonics News **27**(5), 24–31 (2016).
28. M. H. Morsy, "Review and recent developments of laser ignition for internal combustion engines applications," Renew. Sustain. Energy Rev. **16**(7), 4849–4875 (2012).
29. I. A. Salehi, B. C. Gahan, and S. Batarseh, "Laser drilling-drilling with the power of light," Tech. rep., Gas Technology Institute, Des Plaines, IL (United States) (2007).
30. C. Martinet, V. Paillard, A. Gagnaire, *et al.*, "Deposition of sio_2 and tio_2 thin films by plasma enhanced chemical vapor deposition for antireflection coating," J. Non-Cryst. Solids **216**, 77–82 (1997).
31. P. Doshi, G. E. Jellison, and A. Rohatgi, "Characterization and optimization of absorbing plasma-enhanced chemical vapor deposited antireflection coatings for silicon photovoltaics," Appl. Opt. **36**(30), 7826–7837 (1997).
32. G. Womack, K. Isbilir, and F. Lisco, "The performance and durability of single-layer sol-gel anti-reflection coatings applied to solar module cover glass," Surf. Coat. Technol. **358**, 76–83 (2019).
33. K. Guo, Y. Wang, and R. Chen, "Effects of ion beam etching of fused silica substrates on the laser-induced damage properties of antireflection coatings at 355 nm," Opt. Mater. **90**, 172–179 (2019).
34. D. S. Hobbs and B. D. MacLeod, "High laser damage threshold surface relief micro-structures for anti-reflection applications," in *Laser-Induced Damage in Optical Materials: 2007*, vol. 6720 (SPIE, 2007), pp. 204–213.
35. K. Juškevičius, R. Buzelis, and G. Abromavičius, "Argon plasma etching of fused silica substrates for manufacturing high laser damage resistance optical interference coatings," Opt. Mater. Express **7**(10), 3598–3607 (2017).
36. J. van de Groep, P. Spinelli, and A. Polman, "Single-step soft-imprinted large-area nanopatterned antireflection coating," Nano Lett. **15**(6), 4223–4228 (2015).
37. P. Spinelli, M. Verschuuren, and A. Polman, "Broadband omnidirectional antireflection coating based on subwavelength surface mie resonators," Nat. Commun. **3**(1), 692 (2012).
38. K. X. Wang, Z. Yu, and S. Sandhu, "Condition for perfect antireflection by optical resonance at material interface," Optica **1**(6), 388–395 (2014).
39. E. F. Pecora, A. Cordaro, P. G. Kik, *et al.*, "Broadband antireflection coatings employing multiresonant dielectric metasurfaces," ACS Photonics **5**(11), 4456–4462 (2018).
40. M. Bouabdellaoui, S. Checcucci, and T. Wood, "Self-assembled antireflection coatings for light trapping based on sige random metasurfaces," Phys. Rev. Mater. **2**(3), 035203 (2018).
41. P. Spinelli, B. Macco, and M. Verschuuren, "Al_2o_3/tio_2 nano-pattern antireflection coating with ultralow surface recombination," Appl. Phys. Lett. **102**(23), 1 (2013).
42. T. Bottein, T. Wood, and T. David, ""black" titania coatings composed of sol-gel imprinted mie resonators arrays," Adv. Funct. Mater. **27**(2), 1604924 (2017).
43. M. Modaresialam, Z. Chehadi, and T. Bottein, "Nanoimprint lithography processing of inorganic-based materials," Chem. Mater. **33**(14), 5464–5482 (2021).
44. Z. Chehadi, M. Bouabdellaoui, and M. Modaresialam, "Scalable disordered hyperuniform architectures via nanoimprint lithography of metal oxides," ACS Appl. Mater. Interfaces **13**(31), 37761–37774 (2021).
45. S.-H. Hong, B.-J. Bae, and K.-S. Han, "Imprinted moth-eye antireflection patterns on glass substrate," Electron. Mater. Lett. **5**(1), 39–42 (2009).
46. K.-S. Han, J.-H. Shin, and H. Lee, "Enhanced transmittance of glass plates for solar cells using nano-imprint lithography," Sol. energy materials solar cells **94**(3), 583–587 (2010).
47. H. Deniz, T. Khudiyev, F. Buyukserin, *et al.*, "Room temperature large-area nanoimprinting for broadband biomimetic antireflection surfaces," Appl. Phys. Lett. **99**(18), 1 (2011).
48. K.-C. Park, H. J. Choi, and C.-H. Chang, "Nanotextured silica surfaces with robust superhydrophobicity and omnidirectional broadband supertransmissivity," ACS Nano **6**(5), 3789–3799 (2012).
49. H. K. Raut, S. S. Dinachali, and Y. C. Loke, "Multiscale ommatidial arrays with broadband and omnidirectional antireflection and antifogging properties by sacrificial layer mediated nanoimprinting," ACS Nano **9**(2), 1305–1314 (2015).

Optics EXPRESS

50. P. Clapham and M. Hutley, "Reduction of lens reflexion by the "moth eye" principle," Nature **244**(5414), 281–282 (1973).
51. W.-L. Min, B. Jiang, and P. Jiang, "Bioinspired self-cleaning antireflection coatings," Adv. Mater. **20**(20), 3914–3918 (2008).
52. M. Motamedi, M. E. Warkiani, and R. A. Taylor, "Transparent surfaces inspired by nature," Adv. Opt. Mater. **6**(14), 1800091 (2018).
53. M. R. Lotz, C. R. Petersen, and C. Markos, "Direct nanoimprinting of moth-eye structures in chalcogenide glass for broadband antireflection in the mid-infrared," Optica **5**(5), 557–563 (2018).
54. H. Hattori, "Anti-reflection surface with particle coating deposited by electrostatic attraction," Adv. Mater. **13**(1), 51–54 (2001).
55. D. S. Hobbs, B. D. MacLeod, E. Sabatino III, *et al.*, "Contamination resistant antireflection nano-textures in fused silica for laser optics," in *Laser-Induced Damage in Optical Materials: 2013*, vol. 8885 (SPIE, 2013), pp. 61–71.
56. K. Askar, B. M. Phillips, and Y. Fang, "Self-assembled self-cleaning broadband anti-reflection coatings," Colloids Surfaces A: Physicochem. Eng. Aspects **439**, 84–100 (2013).
57. L. E. Busse, C. M. Florea, and J. A. Frantz, "Anti-reflective surface structures for spinel ceramics and fused silica windows, lenses and optical fibers," Opt. Mater. Express **4**(12), 2504–2515 (2014).
58. S. Haghanifar, M. McCourt, and B. Cheng, "Creating glasswing butterfly-inspired durable antifogging superomniphobic supertransmissive, superclear nanostructured glass through bayesian learning and optimization," Mater. Horiz. **6**(8), 1632–1642 (2019).
59. E. Feigenbaum, N. J. Ray, and J.-H. Yoo, "Optical modeling of random anti-reflective meta-surfaces for laser systems applications," Appl. Opt. **58**(27), 7558–7565 (2019).
60. S. Haghanifar, M. McCourt, and B. Cheng, "Discovering high-performance broadband and broad angle antireflection surfaces by machine learning," Optica **7**(7), 784–789 (2020).
61. G. Y. Yoo, N. Nurrosyid, and S. Lee, "Newly developed broadband antireflective nanostructures by coating a low-index mgf_2 film onto a sio_2 moth-eye nanopattern," ACS Appl. Mater. Interfaces **12**(9), 10626–10636 (2020).
62. N. J. Ray, J.-H. Yoo, and H. T. Nguyen, "Substrate-engraved antireflective nanostructured surfaces for high-power laser applications," Optica **7**(5), 518–526 (2020).
63. N. J. Ray, J.-H. Yoo, H. T. Nguyen, *et al.*, "Designer metasurfaces for antireflective applications enabled by advanced nanoparticle technology," Adv. Opt. Mater. **10**(10), 2200151 (2022).
64. N. J. Ray, J.-H. Yoo, and H. T. Nguyen, "Enhanced laser-induced damage performance of all-glass metasurfaces for energetic pulsed laser applications," Appl. Opt. **62**(31), 8219–8223 (2023).
65. N. J. Ray, J.-H. Yoo, H. T. Nguyen, *et al.*, "All-glass metasurfaces for ultra-broadband and large acceptance angle antireflectivity: from ultraviolet to mid-infrared," Adv. Opt. Mater. **11**(12), 2300137 (2023).
66. C.-H. Sun, P. Jiang, and B. Jiang, "Broadband moth-eye antireflection coatings on silicon," Appl. Phys. Lett. **92**(6), 1 (2008).
67. X. Ye, J. Huang, and F. Geng, "High power laser antireflection subwavelength grating on fused silica by colloidal lithography," J. Phys. D: Appl. Phys. **49**(26), 265104 (2016).
68. M. Bochet-Modaresialam, J.-B. Claude, D. Grosso, *et al.*, "Methylated silica surfaces having tapered nipple-dimple nanopillar morphologies as robust broad-angle and broadband antireflection coatings," ACS Appl. Nano Mater. **3**(6), 5231–5239 (2020).
69. A. A. Manenkov and A. M. Prokhorov, "Laser-induced damage in solids," Sov. Phys. Usp. **29**(1), 104–122 (1986).
70. J.-Y. Natoli, L. Gallais, H. Akhouayri, *et al.*, "Laser-induced damage of materials in bulk, thin-film, and liquid forms," Appl. Opt. **41**(16), 3156–3166 (2002).
71. A. A. Manenkov, "Fundamental mechanisms of laser-induced damage in optical materials: today's state of understanding and problems," Opt. Eng. **53**(1), 010901 (2014).
72. T. Bottein, O. Dalstein, and M. Putero, "Environment-controlled sol–gel soft-nil processing for optimized titania, alumina, silica and yttria-zirconia imprinting at sub-micron dimensions," Nanoscale **10**(3), 1420–1431 (2018).
73. R. J. Weiblen, C. Florea, L. Busse, *et al.*, "Increased laser damage threshold in as_2s_3 motheye antireflective structures," in *CLEO: Applications and Technology*, (Optica Publishing Group, 2014), pp. JTh3J–4.
74. R. J. Weiblen, C. M. Florea, and L. E. Busse, "Irradiance enhancement and increased laser damage threshold in as_2 s_3 moth-eye antireflective structures," Opt. Lett. **40**(20), 4799–4802 (2015).
75. F. Liu, H. Jiao, and B. Ma, "Influence of the surface and subsurface contaminants on laser-induced damage threshold of anti-reflection sub-wavelength structures working at 1064 nm," Opt. & Laser Technol. **127**, 106144 (2020).
76. Temicon, "Broadband antireflection over a wide angle with only one layer (https://www.temicon.com/industries/optics),".
77. S. Checcucci, T. Bottein, and M. Gurioli, "Multifunctional metasurfaces based on direct nanoimprint of titania sol–gel coatings," Adv. Opt. Mater. **7**(10), 1801406 (2019).
78. I. Standardization, "Lasers and laser-related equipment. test methods for laser-induced damage threshold. part 1: Definitions and general principles," International Organization for Standardization (2011).
79. M. Stehlík, F. Wagner, and J. Zideluns, "Beam-size effects on the measurement of sub-picosecond intrinsic laser induced damage threshold of dielectric oxide coatings," Appl. Opt. **60**(27), 8569–8578 (2021).
80. I. O. for Standardization, "Lasers and laser-related equipment-test methods for laser-induced damage threshold-part 1: definitions and general principles," tech. rep. ISO 21254-1:2011 pp. 21254–1 (2011).

Optics EXPRESS

81. L. Gallais, J. Capoulade, and J.-Y. Natoli, "Laser damage resistance of hafnia thin films deposited by electron beam deposition, reactive low voltage ion plating, and dual ion beam sputtering," Appl. Opt. **47**(13), C107–C113 (2008).
82. C. Petite, R. Marcouillé, and A. Moreau, "Multipass lock-in thermography for the study of optical coating absorption," Appl. Opt. **61**(4), 978–988 (2022).
83. M. Naffouti, R. Backofen, and M. Salvalaglio, "Complex dewetting scenarios of ultrathin silicon films for large-scale nanoarchitectures," Sci. Adv. **3**(11), eaao1472 (2017).
84. P. Forbes, "Self-cleaning materials," Sci. Am. **299**(2), 88–95 (2008).
85. D. Dodd and D. Fraser, "Optical determinations of oh in fused silica," J. Appl. Phys. **37**(10), 3911 (1966).
86. D. H. Raguin and G. M. Morris, "Antireflection structured surfaces for the infrared spectral region," Appl. Opt. **32**(7), 1154–1167 (1993).
87. M. Steel, T. White, and C. M. De Sterke, "Symmetry and degeneracy in microstructured optical fibers," Opt. Lett. **26**(8), 488–490 (2001).
88. P. F. Belleville, P. Prene, C. Bonnin, *et al.*, "How smooth chemistry allows high-power laser optical coating preparation," in *Advances in Optical Thin Films*, vol. 5250 (SPIE, 2004), pp. 196–202.
89. X. Li, M. Gross, B. Oreb, *et al.*, "Increased laser-damage resistance of sol–gel silica coating by structure modification," RDPC:\Users\jayak\RDP6| **116**(34), 18367–18371 (2012).
90. P. Baisden, L. Atherton, and R. Hawley, "Large optics for the national ignition facility," Fusion Sci. Technol. **69**(1), 295–351 (2016).
91. N. J. Ray, J.-H. Yoo, and H. T. Nguyen, "Birefringent glass-engraved tilted pillar metasurfaces for high power laser applications," Adv. Sci. **10**(24), 2301111 (2023).
92. M. Bollani, M. Salvalaglio, and A. Benali, "Templated dewetting of single-crystal sub-millimeter-long nanowires and on-chip silicon circuits," Nat. Commun. **10**(1), 5632 (2019).
93. M. Salvalaglio, M. Bouabdellaoui, and M. Bollani, "Hyperuniform monocrystalline structures by spinodal solid-state dewetting," Phys. Rev. Lett. **125**(12), 126101 (2020).
94. Y. Du, M. Zhu, and Q. Liu, "Laser-induced damage properties of subwavelength antireflective grating on fused silica," Thin Solid Films **567**, 47–53 (2014).
95. D. Berman, S. Guha, and B. Lee, "Sequential infiltration synthesis for the design of low refractive index surface coatings with controllable thickness," ACS Nano **11**(3), 2521–2530 (2017).
96. L. Gallais and J.-Y. Natoli, "Optimized metrology for laser-damage measurement: application to multiparameter study," Appl. Opt. **42**(6), 960–971 (2003).
97. L. Gallais and M. Commandré, "Laser-induced damage thresholds of bulk and coating optical materials at 1030 nm, 500 fs," Appl. Opt. **53**(4), A186–A196 (2014).
98. L. Gallais, D.-B. Douti, and M. Commandre, "Wavelength dependence of femtosecond laser-induced damage threshold of optical materials," J. Appl. Phys. **117**(22), 1 (2015).
99. R. A. Negres, C. J. Stolz, S. B. DeFrances, *et al.*, "1077-nm, cw mirror thin film damage competition," in *Laser-Induced Damage in Optical Materials 2022*, vol. 12300 (SPIE, 2022), p. 1230002.
100. A. Ribeaud, J. Pistner, M. Soulier, *et al.*, "Study of high-performance ibs coatings for near-ir laser applications," in *Laser-Induced Damage in Optical Materials 2023*, vol. 12726 (SPIE, 2023), pp. 27–33.
101. A. V. Smith and B. T. Do, "Bulk and surface laser damage of silica by picosecond and nanosecond pulses at 1064 nm," Appl. Opt. **47**(26), 4812–4832 (2008).
102. J. P. Nole, "Nanotextured optical surfaces advance laser power and reliability," Laser Focus World **50**, 38–43 (2014).
103. C. V. Thompson, "Solid-state dewetting of thin films," Annu. Rev. Mater. Res. **42**(1), 399–434 (2012).
104. A. N. Zaaf, H. S. Small, T. M. LeRocque, *et al.*, "Impact of a plasma mitigation process on the 266 nm pulsed lidt of rar nano-textured fused silica," in *Laser-Induced Damage in Optical Materials 2022*, vol. 12300 (SPIE, 2022), pp. 66–76.
105. J. Schmitt, A. Meier, U. Wallrabe, *et al.*, "Reactive ion etching (cf 4/ar) and ion beam etching of various glasses for diffractive optical element fabrication," Int. J. Appl. Glass Sci. **9**(4), 499–509 (2018).
106. E. Council, "Fluorinated gases and ozone-depleting substances: Council and parliament reach agreement (https://www.consilium.europa.eu/en/press/press-releases/2023/10/05/fluorinated-gases-and-ozone-depleting-substances-council-and-parliament-reach-agreement/)," (2023).
107. D. N. P. Group, "Nano-imprint lithography (https://www.global.dnp/biz/solution/products/detail/10162425_4130.html)," (2023).

150.217.251.66 {ts '2024-04-05 04:59:57'}